

COMPUTATIONAL SIMULATION OF TURBULENT FLOW IN AN AXIAL COMPRESSOR ROTOR WITH A REYNOLDS STRESS MODEL

Bruno G. Montojos, bgm87@lasme.coppe.ufrj.br

Universidade Federal do Rio de Janeiro, COPPE, Nuclear Engineering Program

Newton R. Moura, newton.moura@petrobras.com.br

Petrobras/CENPES/Gas and Energy

Jian Su, sujian@lasme.coppe.ufrj.br

Universidade Federal do Rio de Janeiro, COPPE, Nuclear Engineering Program

Abstract. *A numerical study was carried out on a rotor of a axial transonic compressor, NASA Rotor 37, in order to show a comparison between the results obtained with the Reynolds Stress turbulence model present in commercial codes of CFD and the experimental data based on a laboratory test. Moreover, the results of a previous and similar study with two-equation turbulence models were used to investigate some discrepancies between the models. Two Reynolds stress turbulence models was applied in the present work, one based on the ϵ -equation and the other, Baseline RSM, based on the ω -equation with a wall function that alternates the model between the ω -equation and the ϵ -equation depending on the proximity of the wall. The simulation results are in good agreement with available experimental data.*

Keywords: *turbomachinery; axial compressor; CFD; turbulence models; RSM*

1. INTRODUCTION

Axial compressors are designed to operate with higher mass flux, better thermodynamic efficiency and moderate pressure ratio in comparison with centrifugal compressors. This class of turbomachinery is applied in medium and large size gas turbine air compressor, and air compressor in the fluid cat craker units (FCC) in the oil industry and even in air blower in the iron and steel industry, which involves a complex turbulent flow field caused by a three-dimensional blade rows geometry, secondary flows and some gaps effects as by the clearance at the blade tip.

The numerical analysis with CFD code in turbomachinery has become very important in its design during the years. According to Denton (1999), computational fluid dynamics probably have the most important role in a turbomachinery project than in any other application in engineering. This tool regards a numerical flow predictability which streamline the hole process of design and optimization of a turbine or a compressor in industry reducing the number of prototypes and experimental tests required for project implementation. However, we need to be cautious, since there are plenty of issues that should be taken into consideration to assure the reliability of the method and the models, otherwise, simulations could show inaccurate results compared with the reality of the studied turbomachinery.

Therefore Dunham (1998) reported the results of a blind test case with the rotor from a transonic compressor, NASA Rotor 37, carried out to investigate the predictability of the CFD codes in turbomachineries. In this test, several specialists implemented all methods and models that best suited them and presented their results without having access to experimental data. The purpose of this test was to provide a better understanding and a broad comparison of the codes and models by exposing its weaknesses to the research community. Through the analysis it was found out that the main issues, responsible for presenting scatter results in CFD simulations were the turbulence models, the CFD methods implemented, the grid treatment and the operator. Each of these points require a prior analysis so that the simulation provides accurate results. For instance, the case of computational cost versus the grid quality, that requires a mesh convergence test; the use of appropriate physical models; and the choice of turbulence models that achieve results closer to reality. The last one is a key point for the reliability of CFD simulation.

Despite all turbulence models improvement in the past two decades, the evaluation requirement of these models remains. This is due to the large number of possibilities to represent the turbulence phenomena, each with its particularity and coverage cases. According to Bardina et al. (1997), the proliferation of models and the lack of information about their performance under different flow conditions create additional uncertainties and risks in the design process. He performed a research to test four turbulence models: eddy-viscosity two equations types Wilcox $\kappa - \omega$, Launder and Sharma $\kappa - \epsilon$, Menter SST and one equation type Spalart and Allmaras, for ten experimental flows which include free-shear flows, attached and separated boundary layers. The best overall method in his study was the SST, good for complex flows with separation, followed by the Spalart and Allmaras, the best regarding the computational cost and also good in complex flows, $\kappa - \epsilon$, the worse when a separated flow is present, however, gave good results for freestream condition, $\kappa - \omega$, poor results due to its sensibility to freestream conditions.

Following the same guidelines, Simoes et al. (2009) presented a work that investigated the evaluation of the turbulent flow inside the NASA Rotor 37. He performed the simulations using the same models as Bardina et al. (1997), except Spalart Allmaras and concluded that the most accurate results were given by SST followed by $\kappa - \epsilon$ and $\kappa - \omega$. This work will perform an extension of Simoes et al. (2009) caring out a CFD simulation based on the Reynold Average Navier

Stokes equation and two Reynolds Stress Turbulence Models to show the validation against experimental data and the previous calculation with the other methods. The performance curves and some local distributions will be presented in this paper with the conclusions taken.

2. TECHNIQUE APPROACH

2.1 Governing equation

2.1.1 SSG-RSM model

In the governing equation, it was considered a three dimensional turbulent flow of a newtonian fluid and constant thermophysical properties. The continuity equation is:

$$\frac{\partial U_i}{\partial x_i} = 0 \quad (1)$$

in which ρ is the specific mass, \mathbf{U} is the velocity vector and t is the time. The Reynolds averaged Navier-Stokes (RANS) equations are given by:

$$\frac{\partial \rho U_i}{\partial t} + \frac{\partial (\rho U_i U_j)}{\partial x_j} - \frac{\partial}{\partial x_j} \left[\mu \left(\frac{\partial U_i}{\partial x_j} + \frac{\partial U_j}{\partial x_i} \right) \right] = \frac{\partial p''}{\partial x_i} - \frac{\partial}{\partial x_j} \rho (\overline{u_i u_j}) + S_{M_i} \quad (2)$$

in which S_{M_i} is the body force vector, that is null in this study, p'' is turbulent modified pressure and $\frac{\partial}{\partial x_j} \rho (\overline{u_i u_j})$ is the fluctuating Reynolds stress contribution.

The main difference between the two equations for the RSM turbulence models is that RSM does not use the eddy viscosity hypothesis. In this case, the models are based on transport equations for all components of the Reynolds stress tensor and the dissipation rate. Therefore instead of two equations it is required to solve a separate equation for each of the six Reynolds stress components of the tensor $\frac{\partial}{\partial x_j} \rho (\overline{u_i u_j})$. The modified pressure, in this case, has no turbulence contribution and is related to the static (thermodynamic) pressure by:

$$p'' = p + \frac{2}{3} \mu \frac{\partial U_k}{\partial x_k} \quad (3)$$

and the differential equation Reynolds stress transport, based in ϵ equation, is:

$$\frac{\partial \rho \overline{u_i u_j}}{\partial t} + \frac{\partial}{\partial x_k} (U_k \rho \overline{u_i u_j}) - \frac{\partial}{\partial x_k} \left(\left(\mu + \frac{2}{3} C_S \rho \frac{\kappa^2}{\epsilon} \right) \frac{\partial \overline{u_i u_j}}{\partial x_k} \right) = P_{ij} - \frac{2}{3} \delta_{ij} \rho \epsilon + \Phi_{ij} + P_{ij,b} \quad (4)$$

in which Φ_{ij} is the pressure-strain correlation, and P_{ij} is the shear turbulence production and is given by:

$$P_{ij} = -\rho \overline{u_i u_k} \frac{\partial U_j}{\partial u_k} - \rho \overline{u_j u_k} \frac{\partial U_i}{\partial u_k} \quad (5)$$

The term $P_{ij,b}$ is the buoyancy turbulent production, given by:

$$P_{ij,b} = B_{ij} - C_{buo} \left(B_{ij} - \frac{1}{3} B_{kk} \delta_{ij} \right) \quad (6)$$

in which the second term represents the buoyancy contribution from the pressure-strain term, and B_{ij} is given by:

$$B_{ij} = g_i b_j + g_j b_i \quad (7)$$

Using the Boussinesq buoyancy model, then b_i is modeled as

$$b_i = \frac{\mu_t \beta}{\sigma_\rho} \frac{\partial T}{\partial x_i} \quad (8)$$

in which β is the thermal expansion coefficient. Could otherwise be used a full buoyancy model based on density differences to model the buoyancy.

$$b_i = \frac{\mu_t}{\sigma_\rho} \frac{\partial \rho}{\partial x_i} \quad (9)$$

As the turbulence dissipation appears in the individual stress equations, an equation for ϵ is still required. This now has the form:

$$\frac{\partial(\rho\epsilon)}{\partial t} + \frac{\partial}{\partial x_k}(U_k\rho U_k\epsilon) = -\frac{\epsilon}{k}(C_{\epsilon 1}P_k - C_{\epsilon 2}\rho\epsilon + C_{\epsilon 1}P_{eb}) + \frac{\partial}{\partial x_k}[(\mu + \frac{\mu_t}{\sigma_{\epsilon}RS})\frac{\partial\epsilon}{\partial x_l}] \quad (10)$$

In these equations, the anisotropic diffusion coefficients of the original models have been replaced by an isotropic formulation, which increases the robustness of the Reynolds stress model. The Reynolds Stress model is also available with anisotropic diffusion coefficients. In this case, the following equations are solved for the transport of the Reynolds stresses:

$$\frac{\partial\rho\overline{u_i u_j}}{\partial t} + \frac{\partial}{\partial x_k}(U_k\rho\overline{u_i u_j}) - \frac{\partial}{\partial x_k}((\delta_{kl}\mu + \rho C_S \frac{k}{\epsilon}\overline{u_k u_l})\frac{\partial\overline{u_i u_j}}{\partial x_l}) = P_{ij} - \frac{2}{3}\delta_{ij}\rho\epsilon + \Phi_{ij} + P_{ij,b} \quad (11)$$

in which Φ_{ij} is the pressure-strain correlation, and P_{ij} , the exact production term, is given by Equation 5. In this case the production due to buoyancy is for the Boussinesq approximation modeled as:

$$b_i = C_S\rho\beta\frac{k}{\epsilon\sigma_p}\overline{u_i u_k}\frac{\partial T}{\partial x_k} \quad (12)$$

Otherwise the term is modeled as (full buoyancy model based on density differences):

$$b_i = -C_S\rho\frac{k}{\epsilon\sigma_p}\overline{u_i u_k}\frac{\partial\rho}{\partial x_k} \quad (13)$$

The equation for ϵ is:

$$\frac{\partial(\rho\epsilon)}{\partial t} + \frac{\partial}{\partial x_k}(U_k\rho U_k\epsilon) = -\frac{\epsilon}{k}(C_{\epsilon 1}P_k - C_{\epsilon 2}\rho\epsilon + C_{\epsilon 1}P_{eb}) + \frac{\partial}{\partial x_k}[(\mu\delta_{kl} + c_{\epsilon}\rho\frac{k}{\epsilon}\overline{u_k u_l})\frac{\partial\epsilon}{\partial x_l}] \quad (14)$$

The pressure strain term can be split into two parts:

$$\Phi_{ij} = \Phi_{ij,1} + \Phi_{ij,2} \quad (15)$$

in which $\Phi_{ij,1}$ is the "slow" term, also known as the return-to-isotropy term, and $\Phi_{ij,2}$ is called the "rapid" term.

The SSG model developed by Speziale, Sarkar and Gatski uses a quadratic relation for the pressure-strain correlation. In order to compare the pressure-strain correlations for the three models, a general form can be derived based on the anisotropy tensor a_{ij} and the mean strain rate tensor and vorticity tensor, S_{ij} and Ω_{ij} respectively. The general form reads:

$$\Phi_{ij,1} = -\rho\epsilon[C_{S1}a_{ij} + C_{S2}(a_{ik}a_{kj} - \frac{1}{3}a_{mn}a_{mn}\delta_{ij})] \quad (16)$$

$$\Phi_{ij,2} = -C_{r1}Pa_{ij} + C_{r2}\rho k S_{ij} - C_{r3}\rho k S_{ij}\sqrt{a_{mn}a_{mn}} + C_{r4}\rho k(a_{ik}S_{jk} + a_{jk}S_{ik} + \frac{2}{3}a_{kl}S_{kl}\delta_{ij}) + C_{r5}\rho k(a_{ik}\Omega_{jk} + a_{jk}\Omega_{ik}) \quad (17)$$

i which

$$a_{ij} = \frac{u_i u_j}{k} - \frac{2}{3}\delta_{ij} \quad (18)$$

$$S_{ij} = \frac{1}{2}(\frac{\partial U_i}{\partial x_j} + \frac{\partial U_j}{\partial x_i}) \quad (19)$$

$$\Omega_{ij} = \frac{1}{2}(\frac{\partial U_i}{\partial x_j} - \frac{\partial U_j}{\partial x_i}) \quad (20)$$

The constants are listed below for SSG model:

$$C_{\mu RS} = 0.1, \sigma_{\epsilon}RS = 1.36, c_s = 0.22, c_{\epsilon} = 0.18, c_{\epsilon 1} = 1.45, c_{\epsilon 2} = 1.83, C_{S1} = 1.7, C_{s2} = -1.05, C_{s1} = 0.9, C_{r1} = 0.8, C_{r3} = 0.65, C_{r4} = 0.625 \text{ and } C_{r5} = 0.2$$

2.1.2 BSL-RSM model

The Baseline Reynolds Stress Model blends between the RSM based on the ϵ -equation near the surface and the ω -equation in the outer region in order to use both models, in which they present better performance. It consists of a transformation of the RSM based on the ϵ -equation model to the RSM based on the ω -equation formulation by a blending function F_1 used in the RSM equation, which is equal to one near the surface and decreases to a value of zero outside the boundary layer.

So the differential equation Reynolds stress transport, based in ω -equation, is:

$$\frac{\partial \overline{\rho u_i u_j}}{\partial t} + \frac{\partial}{\partial x_k} (U_k \overline{\rho u_i u_j}) - \frac{\partial}{\partial x_k} \left(\left(\mu + \frac{\mu_t}{\sigma_k} \right) \frac{\partial \overline{u_i u_j}}{\partial x_k} \right) = P_{ij} - \frac{2}{3} \beta' \rho \omega k \delta_{ij} + \Phi_{ij} + P_{ij,b} \quad (21)$$

The production due to buoyancy is modeled in the same way as in the RSM based on the ϵ -equation.

To model the turbulence frequency, ω , the following equation is used:

$$\frac{\partial (\rho \omega)}{\partial t} + \frac{\partial (U_k \rho \omega)}{\partial x_k} = \alpha \rho \frac{\omega}{k} P_k + P_{\omega b} - \beta \rho \omega^2 + \frac{\partial}{\partial x_k} \left[\left(\mu + \frac{\mu_t}{\sigma} \right) \frac{\partial \omega}{\partial x_k} \right] \quad (22)$$

In the Baseline RSM model the coefficients α and β of the ω -equation, as well as both the turbulent Prandtl numbers σ^* and σ , are blended between values from the two sets of constants, corresponding to the ω -based model constants and the ϵ -based model constants transformed to an ω -formulation:

$$\frac{\partial (\rho \omega)}{\partial t} + \frac{\partial (U_k \rho \omega)}{\partial x_k} = \alpha_3 \rho \frac{\omega}{k} P_k + P_{\omega b} - \beta_3 \rho \omega^2 + \frac{\partial}{\partial x_k} \left[\left(\mu + \frac{\mu_t}{\sigma_{\omega 3}} \right) \frac{\partial \omega}{\partial x_k} \right] + (1 - F_1) 2\rho \frac{1}{\sigma_2} \frac{\partial k}{\partial x_k} \frac{\partial \omega}{\partial x_k} \quad (23)$$

Thus for the ω zone the coefficients are:

$$\begin{aligned} \sigma_1^* &= 2 \\ \sigma_1 &= 2 \\ \beta_1 &= 0.075 \\ \alpha_1 &= 0.553 \end{aligned}$$

And for the ϵ zone:

$$\begin{aligned} \sigma_1^* &= 1.0 \\ \sigma_1 &= 0.856 \\ \beta_1 &= 0.0828 \\ \alpha_1 &= 0.044 \end{aligned}$$

The blending of coefficients is done by smooth linear interpolation with the same weight function F as the one used in a cross-diffusion term of the ω -equation 23:

$$\phi_3 = F\phi_1 + (1 - F)\phi_2 \quad (24)$$

in which $F = \tanh(\arg^4)$ with:

$$\arg = \min \left\{ \max \left(\frac{\sqrt{k}}{\beta' \omega y}, \frac{500\nu}{y^2} \right), \frac{4\rho k}{CD_{k\omega k - \epsilon} y^2} \right\} \quad (25)$$

and

$$CD_{k\omega} = \max \left\{ 2\rho \frac{1}{\sigma_{k-\epsilon} \omega} \frac{\partial k}{\partial x_j} \frac{\partial \omega}{\partial x_j}, 10^{-10} \right\} \quad (26)$$

For the pressure strain the constitutive relation is given by:

$$\phi_{ij} = \beta' C_1 \rho \omega (-\overline{u_i u_j} + \frac{2}{3} k \delta_{ij}) - \hat{\alpha} (P_{ij} - \frac{2}{3} k \delta_{ij}) - \hat{\beta} (D_{ij} - \frac{2}{3} k \delta_{ij}) - \hat{\gamma} \rho k (S_{ij} - \frac{1}{3} S_{kk} \delta_{ij}) \quad (27)$$

The production tensor of Reynolds stresses is given by:

$$P_{ij} = -\overline{\rho u_i u_k} \frac{\partial U_j}{\partial x_k} - \overline{\rho u_j u_k} \frac{\partial U_i}{\partial x_k}; \quad P = 0.5 P_{kk} \quad (28)$$

The tensor D_{ij} , participating in the pressure-strain model 27, differs from the production tensor in the dot-product indices:

$$D_{ij} = -\overline{\rho u_i u_k} \frac{\partial U_k}{\partial x_j} - \overline{\rho u_j u_k} \frac{\partial U_k}{\partial x_i}; P = 0.5 P_{kk} \quad (29)$$

The turbulent viscosity in the diffusion terms of the balance equations 21 and 22 is calculated in the same way as in the Wilcox model. For details, see The Wilcox k-omega Model.

$$\mu_T = \rho \frac{k}{\omega} \quad (30)$$

and the coefficients for the model are:

$$\begin{aligned} \beta' &= 0.09 \\ \hat{\alpha} &= (8 + C_2)/11 \\ \hat{\beta} &= (8C_2 - 2)/11 \\ \hat{\gamma} &= (60C_2 - 4)/55 \\ C_1 &= 1.8 \\ C_2 &= 0.52 \end{aligned}$$

The mathematical model was solved numerically by using the commercial CFD package ANSYS CFX-12.1. This program uses numerical method of finite volume as solution (Element Based Finite Volume Method - EBFVM), which allows the solution of problems by blending unstructured grids. Then, it is possible to obtain a numerical solution of discretized momentum and mass balance equations.

2.2 NASA Rotor 37

The Rotor 37 was designed as one from four stages intended to cover a range of design parameters typical of aircraft turbine engine high-pressure (core) compressor inlet stages in a research programme. No inlet guide vans were specified and the test was executed for each stage isolated at NASA Lewis Research Center. Figure 1 show the sections in the meridional plane in which the experimental data were measured using aerodynamic probes and laser anemometer. The main parameters of the Rotor 37 are shown in table 1.

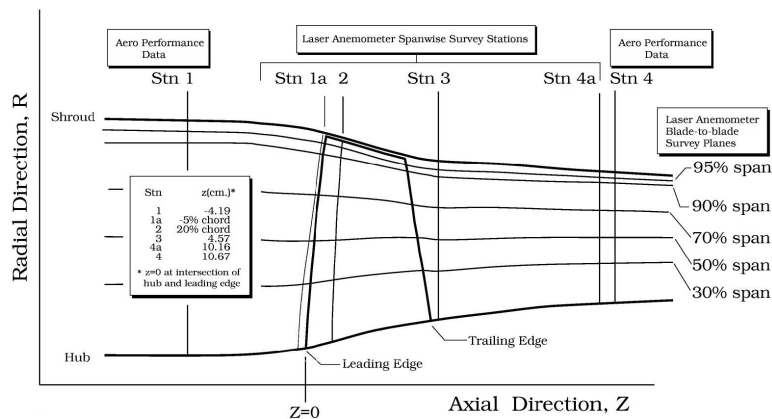


Figure 1. Meridional view form Rotor 37 showing the sections where the experimental data was acquired

3. COMPUTATIONAL DOMAIN, GRID SPECIFICATION AND BOUNDARY CONDITIONS

The domain model followed the test case specifications, showed in the figure 1. The extension of the fluid passage, in the domain, comprehends the hole length from station 1, the inflow boundary, to station 4, the outflow boundary. A convergence test was conducted with some meshes generated for the work. In table 2 were disposed the main control parameters of the mesh used in the test. Two softwares were used in mesh generation, the ICFM CFD and the Turbogrid. The main difference between these softwares is how much control the user has in the parameterization of the mesh. In this case, the ICFM allows greater pliancy than Turbogrid. This flexibility is suitable for the user since it allows a more detailed mesh, on the other hand, gives him less control of all parameters.

A sample of the grid configuration can be seen in the figures 2, 3 and 4. This grid consists of 163 nodes in the streamwise direction, 58 nodes in the blade-to-blade direction and 75 nodes in the spanwise direction. The tip clearance is present in the domain and is described by 12 nodes in the spanwise direction to calculate the secondary flow in this region.

Table 1. Parameters of NASA Rotor 37

Parameter	Value
Number of rotor blades	36
Angular velocity [<i>rpm</i>]	17188.7
Mass flow rate in the choke [<i>Kg/s</i>]	20.93
Total pressure ratio	2.106
Blade tip speed [<i>m/s</i>]	454.14
Tip clearance [<i>cm</i>]	0.0356
Rotor tip relative inlet Mach number	1.48
Rotor hub relative inlet Mach number	1.13
Rotor inlet hub-to-tip diameter ratio	0.7
Rotor tip solidity	1.29

Table 2. Generated Grids

Malha	Software	Elements	Topology	Elements at the Tip	y+
m1	TGrid	0.7M	J Grid	4	3.3
m2	TGrid	1.2M	J Grid	16	6.1
m3	TGrid	2.1M	J Grid	8	0.6
m4	Icem	1.4M	J Grid	12	25.5
m5	Icem	2.0M	H Grid	30	13.5
m6	Icem	2.2M	J Grid	12	0.3

A non-slip condition was imposed on the velocities along the blade and rotor’s walls surfaces. As the inflow condition was defined, the temperature and the total pressure with the velocity direction of the flow normal to the inlet surface where the entrance was non-rotational. A condition of periodicity was defined on the surfaces of up and down the domain toward the blade to blade direction. For the outflow were defined two diferents conditions, the mass flow rate and the static pressure both in the operating point. The static pressure distribution was obtained with the specification of the static pressure at the hub wall and then the simplified radial equilibrium momentum equation,

$$\frac{\partial p}{\partial r} = \rho \frac{v_{\theta}^2}{r} \tag{31}$$

was used to integrate a specified hub exit static pressure in the radial direction.

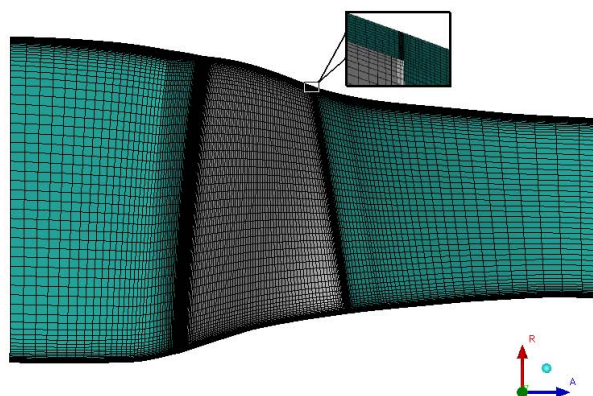


Figure 2. Meridional view of grid configuration with the tip region detailed.

4. CONVERGENCE TEST

Before analysing the case a test was conducted in order to check the convergence of the results and establish the most suitable software for mesh generation. A total of 6 meshes were selected and the grid features varied for the test can be seen in table 2 as the elements density, topology and the elements’ number at the tip clearance and the ogrid topology, which is located around the blade to improve the calculations at this region.



Figure 3. Grid in 70% of span.

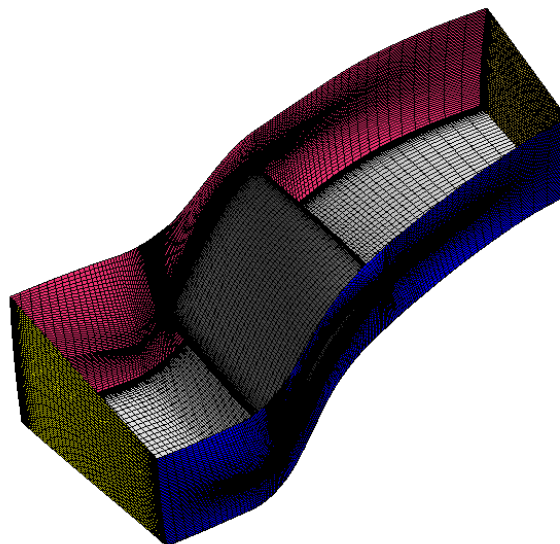


Figure 4. Three dimensional view of grid configuration.

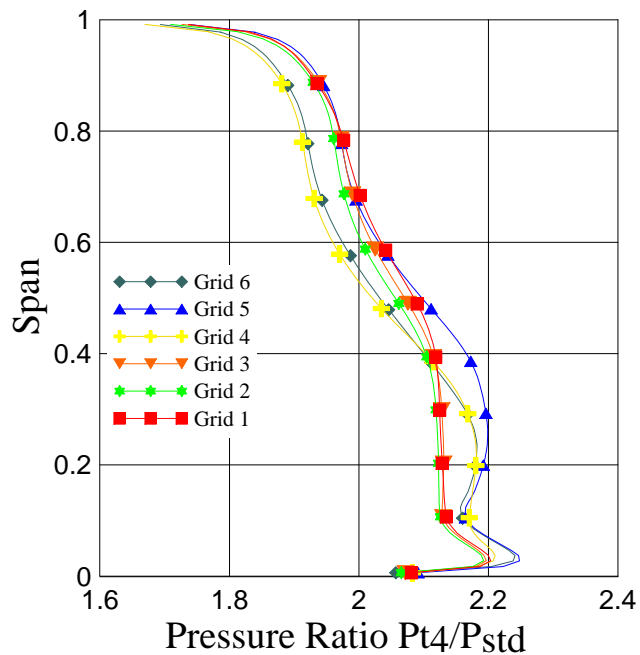


Figure 5. Spanwise distribution of the pressure ratio for the convergence test.

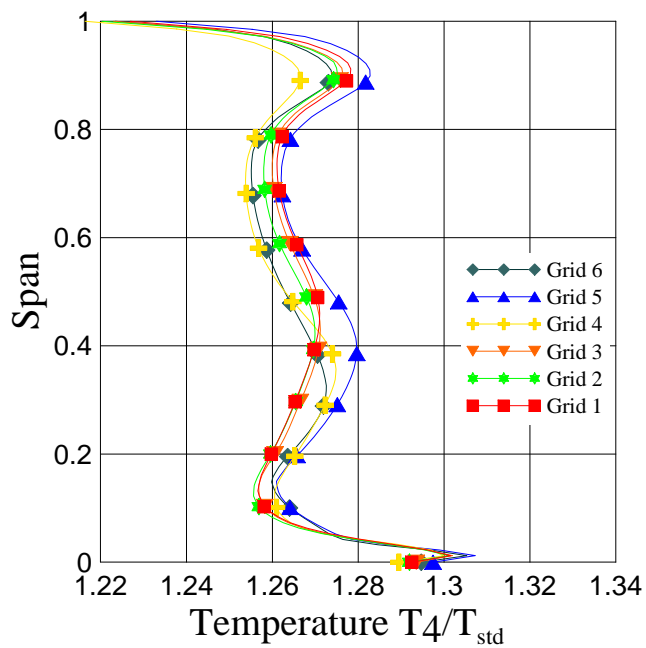


Figure 6. Spanwise distribution of the normalized temperature for the convergence test.

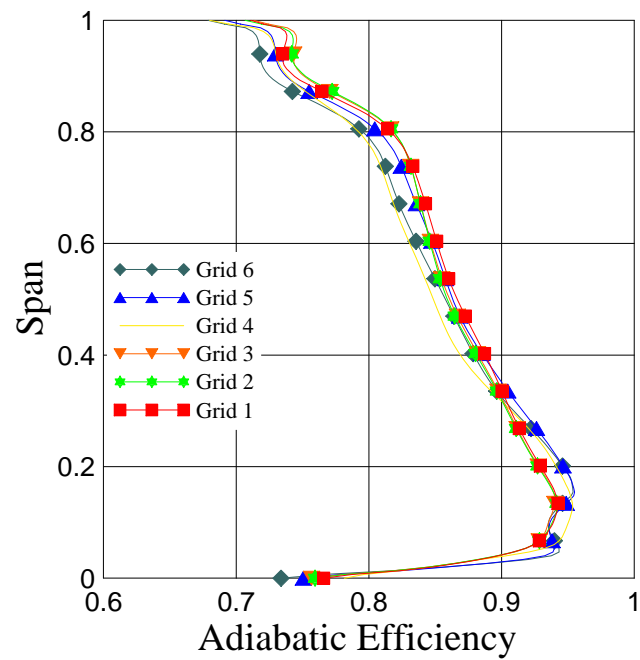


Figure 7. Spanwise distribution of the adiabatic efficiency for the convergence test.

Figures 5, 6 and 7 show the spanwise profile of the total pressure ratio. It is possible to see from pressure and temperature profiles that for the grids generated at the Turbogrid the discrepancies among the curves are not so relevant with a maximum difference of 2%. Regarding the same curves for the meshes generated at the ICEM, it is not possible to assure that the grid convergence was achieved. That can be explained by the fact that the mesh generation in the ICEM CFD demands greater effort to control the parameters in complex geometries.

The curve of adiabatic efficiency showed the Turbogrid's mesh has converged as well as the ICEM meshes, besides the discrepancy of 7 % that could be seen after 90 % of span, close the blade tip region. Nevertheless, regarding the other curves, the ICEM grids were considered not unreliable. So all the simulations used in the analysis were carried out with the domain modeled by grid 1.

5. RESULTS AND DISCUSSION

The purpose of this research was to analyse the reliability of the Reynolds Stress Turbulence Model available in a CFD commercial package in turbomachineries through the simulation of the transsonic axial compressor NASA Rotor 37, contrasting the results with the experimental data and previous simulations with other turbulence models.

In comparison to the eddy-viscosity two equations models, this turbulence model showed more difficulties to converge to reasonable solutions. It was necessary to treat the initial conditioal of the simulation. The false timestep, used to under-relax the equations, and the mass flow rate was controled with the interation in order to stabilize the simulatjons.

Table 3. Generated Grids

Simulation	Mass Flux [Kg/s]	MF Error [%]	Pressure Ratio p_4/p_{std}	PR Error [%]	η_a	η_a Error [%]
SST - m	20.511	—	2.058	2.28	86,1	2.0
SSG - m	20.511	—	1.980	5.96	85,6	2.6
BSL - m	20.511	—	2.041	3.11	85,9	2.3
SST - p	20.175	1,64	2.082	1.16	85,5	2.8
BSL - p	19.984	2,57	2.074	1.53	84,9	3.4
Experimentl	20.511	—	2.106	—	87.9	—

Table 3 shows some operation parameters obtained with the simulations. A total of five simulations are shown, three turbulence models (SST, SSG-RSM and BSL-RSM) and two boundary conditions (mass flux "m" and static pressure "p") were used. The SST followed by the BSL-RSM was in good agreement with the experimental data. For the simulations using the mass flux as outflow boundary condition the SST configured the best result for the computed pressure ratio with a deviation of 2.28 from the experimental data followed by BSL-RSM with a deviation of 3.11 %. This pressure ratio is obtained with the mass average total pressure at the outflow boundary (standard pressure), station 4, over the total pressure at the domain entrance, station 1. Regarding the simulations with the outflow boundary condition with static pressure the computed mass flow for the SST underestimated the experimental results about 1.6 % while BSL underestimated about 2.6 % and SSG-RSM model showed the poorest result. The obtained pressure ratio in this case showed a closer result than the simulations with the mass flux as outflow boundary condition, the SST presented better agreement with the experimental data with 1.16 % of discrepancy, while the BSL model presented 1.53 % of error. Comparing the adiabatic efficiency the results calculated with the mass flux showed the best results with a sharp difference among the turbulence models, but the best result has already been presented by the SST followed by the BSL and the SSG, with a underestimation of 2.0 %, 2.3 % and 2.6 % respectively.

Figure 8 shows the pressure ratio profile at the station 4 for the five simulations from the table 3 and the experiment. The results from the simulations with the static pressure as outflow condition showed the best results with a better experimental agreement for SST, followed closely by BSL-RSM, with a sharp underestimation from 60 % of the span up to the shroud wall. The simulations with mass flux as outflow condition for SST and BSL-RSM underestimated the experimental curve from 40 % of the span up to the shroud wall.

The temperature profiles presented by figure 8 showed thr opposite behavior of pressure profiles. The best results were presented by the simulations with the mass flux as the outflow condition. The results from SST simulation showed best agreement with the experimental data with sharps deviation from experimental curve btween 10 % and 90 % of the span. The BSL presented results quite underestimated between 40 % and 80 %. Again SSG showed the poorest result, underestimating a lot the experimental data. The simulations with static pressure superestimated the experimental curves with a more marked discrepancy from 40 % up to the shroud wall.

Regarding adiabatic efficiency curve, all models showed a good agreement with the experimental curve until 40 % of the span. After that, the adiabatic efficiency is lower then the experimental data, which corresponds an underestimation of the total pressure in this region.

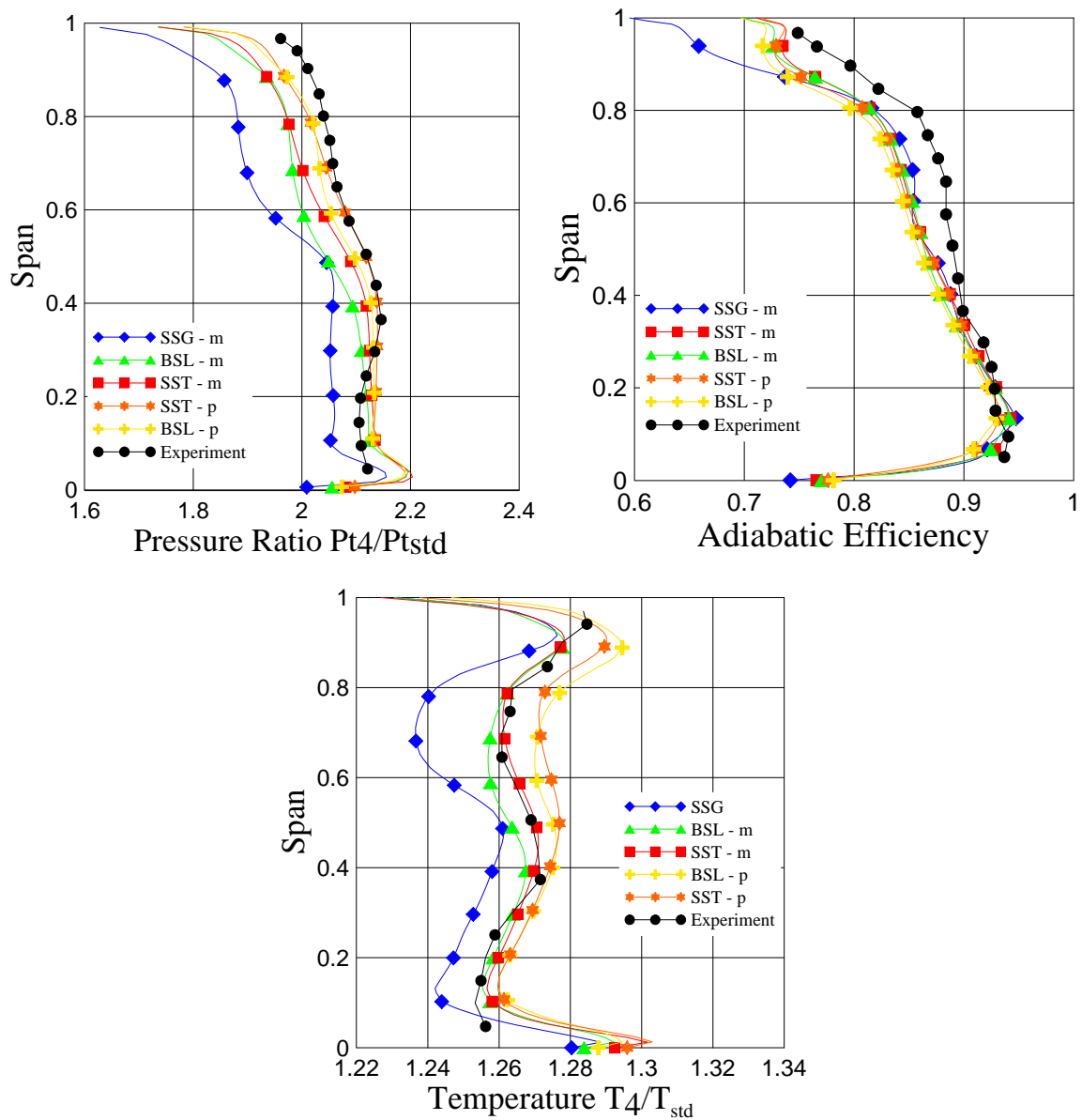


Figure 8. Spanwise distribution of the pressure ratio, temperature and the adiabatic efficiency.

Figure 10 shows the contours of relative mach number located at 50% of the span. It shows the effect of the bow shock waves attached to the leading edge reaching the suction side of the other blade on 50% of the chord approximately. With the drop in velocity, after this wave, there is an increase in pressure.

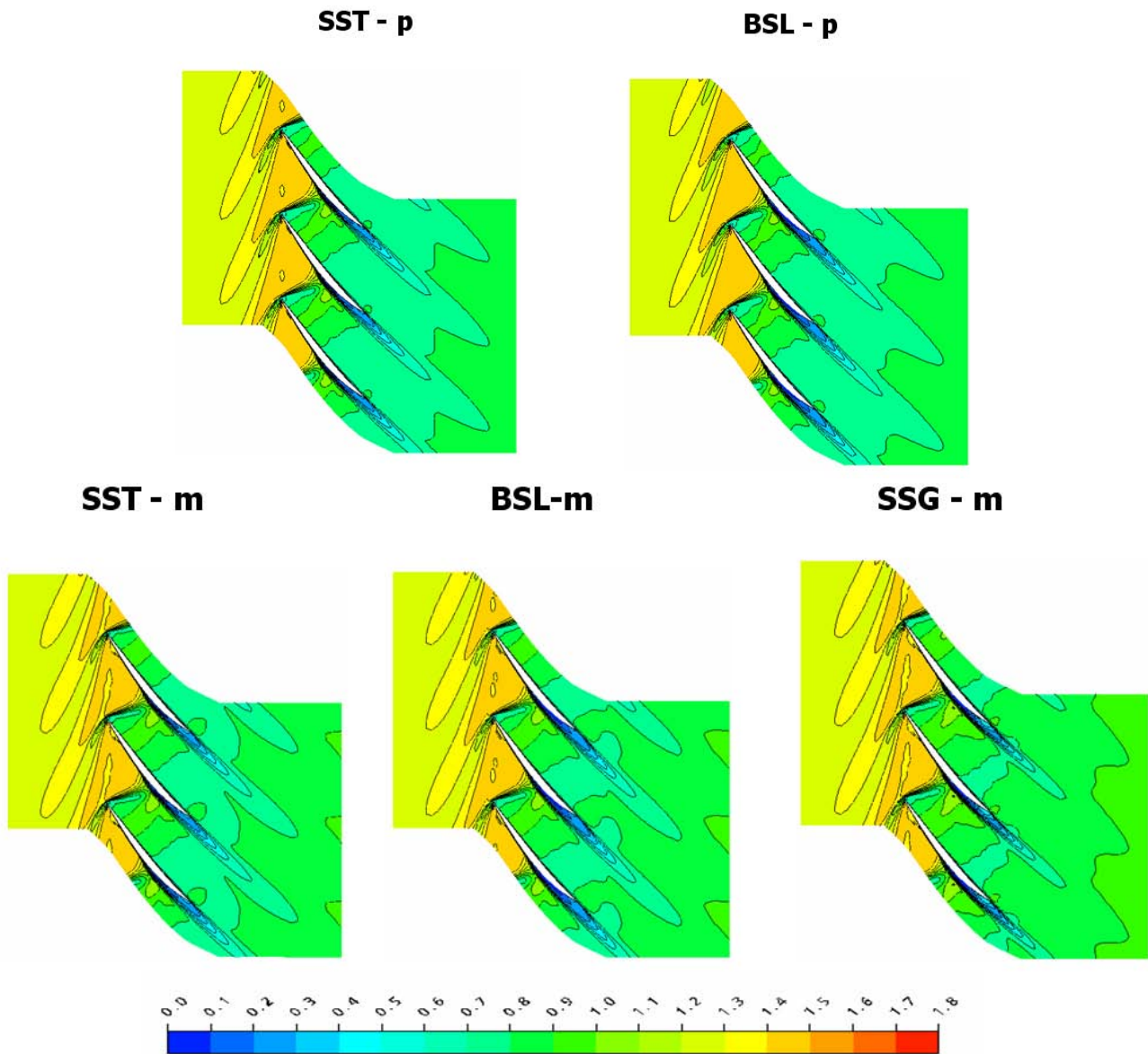


Figure 9. Contour of relative mach number in 50 % of span.

A strong radial gradient of the velocity could be seen in figure 10 at the blade surface in the suction zone, in which the streamlines show the corner stall. There is a limit between this radial movement and the flow where the bow shock wave reaches the blade. All the models showed the same movement and close values but SSG-RSM model, which presented a higher velocity close to the leading edge. At this region the air is convected away from the hub and the flow separates. This separation can be seen in figure 9 in the region with the lowest mach number at the trailing edge. Calculations have shown a separation zone sharper than in the experimental measurements even more for the calculations with the SSG-RSM model. The other models presented similar results among it, with a lower exit velocity and superior pressure.

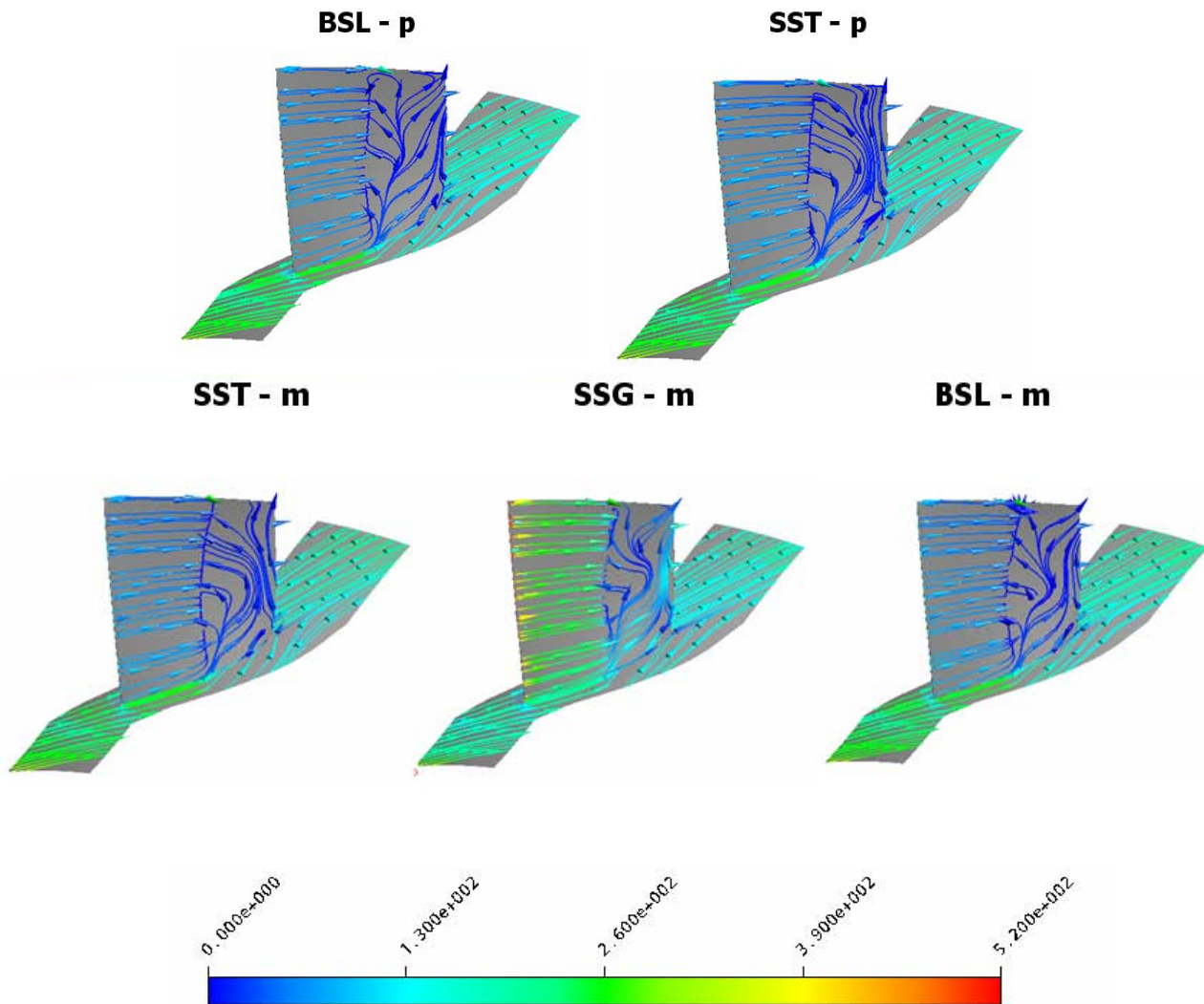


Figure 10. Countour of static pressure in 50 % of span.

6. CONCLUSION

The main purpose of this research was to analyse the performance of a transsonic axial compressor rotor by applying a commercial code and compare different turbulence models and different boundary conditions. The models applied were the two equation SST and two variants of the Reynolds Stress Model, SSG (based on ϵ -equation) and Baselin (based on ω -equation with a wall function to alternate to ϵ -equation).

The simulations of this work were performed in a cluster with 4 nodes with 4 cores each on a speed of 2661 MHz. The simulation time varied with the turbulence models used. The RSM models presented a superior difficulty of convergence, it was necessary to control some parameters with the iterations, as the mass flux and rotational speed, in order to stabilize the simulation to reach acceptable residues which demands a longer time. In addition it was used the results of other simulations as initial conditions to help the convergence too. The SST model presented a faster and less complex convergence, what is common for the eddy viscosity turbulence models.

In order to compare the calculated results with the experimental data the first results analysed was the performance parameters, which showed better results for the SST model followed closely by the BSL model, the SSG was the poorest model analysed showing the superior deviations from the measurements. The same comparison are made with the profiles analysis. The SST presented the closest results with the experimental curves, the BSL also showed good agreement and the SSG showed a great deviation from the experimental curves.

Regarding the outflow boundary condition, the mass flux presented as result a most underestimated pressure ratio than in the simulations using the static pressure profile. This fact is better noticed in the pressure profile curve where for the simulations using the mass flux showed curves with the same shape as the experimental curve but in a lower pressure position in the chart. The simulations using the static pressure showed a result very close with some deviations near to the rotor's hub and shroud. As a conclusion for that behavior of the results is that with the changes of the outflow boundary

condition the operating point is translated at performance curve. When the mass flux is used, the pressure ratio is more underestimated than with the use of static pressure, however, the mass flux is lower than the experimental measurement for the same operating point. For instance, the calculation for the BSL model presented a mass flux with 2.57 % lower than the mass flux in the operating condition and the pressure ratio overcame the calculations of the simulations with the static pressure as boundary condition coming close to the experimental measurements.

As a conclusion the Baseline Reynolds Stress Turbulence Model (RSM-BSL) is validated for the Rotor 37 case and it is a reliable choice for the use of CFD in turbomachinery mainly in compressors, likewise the SST model. Presenting very poor results in comparison to experimental data the SSG model was considered unreliable for the Rotor's 37 case and a any compressor.

7. ACKNOWLEDGEMENTS

The authors acknowledge gratefully financial support provided by CNPQ and Petrobras during the realization of this work.

8. REFERENCES

- Bardina, J. E., Huang, P. G., and Coakley, T. J. (1997). Turbulence modeling validation, testing, and development. *Technical report, NASA TM 110446*.
- Denton, J. D. e Dawes, W. N. (1999). Computational fluid dynamics for turbomachinery design. *Proceedings of the Institution of Mechanical Engineers Part C-Journal of Mechanical Engineering Science*, 213(2):107-124.
- Dunham, J. (1998). Cfd validation for propulsion system components. *Technical report, AGARD-AR-355*.
- Simoës, M. R., Montojos, B. G., Moura, N. R., and Su, J. (2009). Validation of turbulence models for simulation of axial flow compressor. *Proceedings of 20th International Congress of Mechanical Engineering, November 15-20, 2009, Gramado, RS, Brazil*.